Improved hybrid Allen-Cahn phase-field-based lattice Boltzmann method for incompressible two-phase flows

Xi Liu, Zhenhua Chai,* and Baochang Shi
School of Mathematics and Statistics, Huazhong University of Science and Technology, Wuhan, 430074, China;
Institute of Interdisciplinary Research for Mathematics and Applied Science,
Huazhong University of Science and Technology, Wuhan, 430074, China;
and Hubei Key Laboratory of Engineering Modeling and Scientific Computing,
Huazhong University of Science and Technology, Wuhan, 430074, China

(Received 25 November 2022; accepted 16 March 2023; published 29 March 2023)

In this work we develop an improved phase-field based lattice Boltzmann (LB) method where a hybrid Allen-Cahn equation (ACE) with a flexible weight instead of a global weight is used to suppress the numerical dispersion and eliminate the coarsening phenomenon. Then two LB models are adopted to solve the hybrid ACE and the Navier-Stokes equations, respectively. Through the Chapman-Enskog analysis, the present LB model can correctly recover the hybrid ACE, and the macroscopic order parameter used to label different phases can be calculated explicitly. Finally, the present LB method is validated by five tests, including the diagonal translation of a circular interface, two stationary bubbles with different radii, a bubble rising under the gravity, the Rayleigh-Taylor instability in two-dimensional and three-dimensional cases, and the three-dimensional Plateau-Rayleigh instability. The numerical results show that the present LB method has a superior performance in reducing the numerical dispersion and the coarsening phenomenon.

DOI: 10.1103/PhysRevE.107.035308

I. INTRODUCTION

The multiphase flows are universal and important in both nature and industrial processes; however, modeling such flows is a rather challenging work due to the topological changes of the interface among different phases. The phase-field method [1], as one of widely used techniques in the study of multiphase flows, has received increasing attention for its distinct advantages in capturing the complex interface. In this method, a nonzero but thin diffuse interface is adopted to replace the sharp interface among different phases, and the fluid properties vary smoothly across the diffuse interface.

There are two basic kinds of interface-capturing equations commonly used in the phase-field method: the Cahn-Hilliard equation (CHE) [2] and the Allen-Cahn equation (ACE) [3]. In the CHE, the chemical potential based on the phase field theory is introduced into the diffusion term, but a fourth-order spatial derivative leads to a reduction in the locality and the accuracy. As an alternative, the second-order ACE is also used to capture the interface, but the original ACE cannot preserve the total mass conservation [3]. Later, several different solutions have been proposed to overcome the problem. The first one is to introduce a Lagrange multiplier to enforce the total mass conservation, which gives rise to the nonlocal ACE [4]. However, the nonlocal ACE involves the coarsening process, and it will lead to the smaller bubbles disappearing when bubbles with different radii coexist. The second one is to bring a counterterm related to local spacial derivatives into the original ACE to preserve the total mass conservation, and this leads to the popular local ACE [5,6]. Although the local ACE can ensure the mass conservation, it suffers from the numerical dispersion, which may also influence the accuracy of numerical results in the bulk region [7–9]. The third one is to develop the hybrid ACE with a combination of the local and nonlocal ACEs such that the problems of mass conservation and numerical dispersion can be addressed. To this end, Hu *et al.* [8] first proposed a hybrid ACE by using a single global weight to couple the local and nonlocal ACEs. The results showed that the hybrid ACE not only can reduce the numerical dispersion better as compared with local ACE, but also can capture the small features of a complex interface as compared with the nonlocal ACE. Nonetheless, due to use of a single global weight, the hybrid ACE still inherits the coarsening process from the nonlocal ACE, in which the smaller bubbles are unavoidably transferred to the bigger ones. Based on this work, Kang and Yun [9] further developed a local hybrid ACE through adopting a local weight, and it is also found that the numerical dispersion and the coarsening phenomenon can be suppressed. The lattice Boltzmann (LB) method [10–15], as one of mesoscopic numerical approaches, has been developed into a powerful numerical tool [7–9,16–20] for its distinct advantages in kinetic backgrounds, treatment of complex boundary conditions, and computational efficiency in parallel systems. In the framework of the LB method, most of early works [17,21,22] mainly focused on the CHE for its property in mass conservation; nevertheless from a theoretical point of view, the CHE is a fourth-order partial differential equation and cannot be recovered from the second-order LB method. For this reason, the

*Corresponding author: hustczh@hust.edu.cn

second-order conservative ACE is also considered. Geier *et al.* [23] first proposed a local ACE-based LB model (hereafter ACE-LB model) and found that the ACE-LB model has a high-order convergence rate in space than the CHE-based LB model (hereafter CHE-LB model); however, this model cannot recover the local ACE correctly [23]. Based on the above work [23], Ren *et al.* [7] and Wang *et al.* [16] independently developed two improved LB models and demonstrated that the local ACE can be recovered correctly through the Chapman-Enskog analysis. On the other hand, Chai *et al.* [24] presented a LB model for the nonlocal ACE and conducted a comparative study of the local and nonlocal ACE-LB models. They found that the nonlocal ACE-LB model is more stable than the local ACE-LB model, but it cannot preserve the small features of system. To reduce the numerical dispersion in the local ACE-LB model, Hu *et al.* [8] constructed a hybrid ACE-LB model where a global weight is used to combine the local and nonlocal ACEs. The results showed that compared to the local ACE-LB model, the hybrid ACE-LB model can reduce the numerical dispersion, but the coarsening process inherited in the nonlocal ACE-LB cannot be removed. Recently, Kang and Yun [9] developed another hybrid ACE-LB model to suppress the coarsening phenomena through introducing a local weight. Here it should be noted that the local weight depends on the estimation of interface region; to this end, the morphological dilation is adopted, but it would be a difficult task to estimate the interface region for the three-dimensional problem.

To reduce the numerical dispersion and to solve the coarsening problem, in this work we first develop an improved hybrid ACE with a flexible weight, in which the diffusion of the order parameter in the bulk region is controlled by the nonlocal term, while in the interface region, it is governed by the local term. Different from the morphological dilation used in the available work [9], the flexible weight adopted here is related to the signed distance function where its estimation is easier even for three-dimensional problem. Then we propose an improved hybrid ACE-LB method for incompressible two-phase flows, and the order parameter can be calculated explicitly. The rest of the paper is organized as follows. In Sec. II the phase-field theory-based governing equations for incompressible two-phase flows are presented, and followed by the corresponding multiple-relaxation-time (MRT) LB method for these governing equations in Sec. III. In Sec. IV we test the hybrid ACE-LB method with five numerical examples. Finally, some conclusions are given in Sec. V.

II. GOVERNING EQUATIONS

A. The nonlocal ACE with mass conservation

In the phase-field theory, the free energy density of a system can be written as

$$f(\phi, \nabla\phi) = \frac{\kappa}{2}|\nabla\phi|^2 + \psi(\phi), \tag{1}$$

where the first term $\kappa|\nabla\phi|^2/2$ is gradient energy, and the second term $\psi(\phi)$ is bulk energy for a two-phase system. Usually, the bulk energy can be approximated by

$$\psi(\phi) = \beta(\phi_A - \phi)^2(\phi - \phi_B)^2. \tag{2}$$

Here ϕ is the order parameter, and $\phi_{A,B}$ is used to label different phases. Based on the free energy density $f(\phi, \nabla\phi)$, the mixing energy $F(\phi, \nabla\phi)$ and chemical potential μ can be also given by

$$F(\phi, \nabla\phi) = \int_\Omega f(\phi, \nabla\phi)d\Omega = \int_\Omega \left[\frac{\kappa}{2}|\nabla\phi|^2 + \psi(\phi)\right]d\Omega, \tag{3}$$

$$\mu = \frac{\delta F}{\delta\phi} = -\kappa\nabla^2\phi + \psi'(\phi), \tag{4}$$

where Ω is the physical domain, and $\psi'(\phi) = 4\beta(\phi - \phi_A)(\phi - \phi_B)[\phi - (\phi_A + \phi_B)/2]$ is the derivative of function ψ with respect to ϕ. The parameters β and κ are related to the surface tension coefficient σ and interfacial thickness W through $\beta = 12\sigma/W$ and $\kappa = 3\sigma W/2$. Based on the phase-field theory, the dynamics of the order parameter ϕ can also be described by [25]

$$\phi_t + \nabla\cdot(\phi\mathbf{u}) = -M\mu, \tag{5}$$

where M is the mobility. It should be noted that the original ACE (5) cannot conserve the mass of system under the appropriate boundary conditions ($\mathbf{n}\cdot\mathbf{u}|_{\partial\Omega} = 0$ and $\mathbf{n}\cdot\nabla\phi = 0$). To overcome this problem, Rubinstein and Sternberg [4] introduced a nonlocal Lagrange multiplier $\beta_0(t)$ and obtained the following nonlocal ACE:

$$\begin{aligned}&\phi_t + \nabla\cdot(\phi\mathbf{u})\\ &= M\left[\nabla^2\phi - \frac{4\beta}{\kappa}(\phi - \phi_A)(\phi - \phi_B)\left(\phi - \frac{\phi_A + \phi_B}{2}\right)\right.\\ &\quad\left.+\beta_0(t)(\phi_A - \phi)(\phi - \phi_B)\right],\end{aligned} \tag{6}$$

and $\beta_0(t)$ is defined as

$$\beta_0(t) = \frac{\int_\Omega \frac{4\beta}{\kappa}(\phi - \phi_A)(\phi - \phi_B)\left(\phi - \frac{\phi_A+\phi_B}{2}\right)d\mathbf{x}}{\int_\Omega(\phi_A - \phi)(\phi - \phi_B)\,d\mathbf{x}}. \tag{7}$$

Based on the definition of $\beta_0(t)$, it is easy to show the property of mass conservation,

$$\frac{d}{dt}\int_\Omega \phi\,d\mathbf{x} = 0. \tag{8}$$

B. The local ACE with mass conservation

Based on the previous work [5], the order parameter ϕ can also be governed by the following interface advection equation:

$$\phi_t + (u_n\mathbf{n} + \mathbf{u})\cdot\nabla\phi = 0, \tag{9}$$

where $\mathbf{u}$ is the velocity, and $\mathbf{n}$ and u_n are the unit normal vector and normal interface speed, which are given by

$$\mathbf{n} = \frac{\nabla\phi}{|\nabla\phi|}, \quad u_n = -Mk_0. \tag{10}$$

Here k_0 is the interface curvature, and it is defined as

$$k_0 = \nabla\cdot\mathbf{n} = \nabla\cdot\left(\frac{\nabla\phi}{|\nabla\phi|}\right) = \frac{1}{|\nabla\phi|}\left[\nabla^2\phi - \frac{(\nabla\phi\cdot\nabla)|\nabla\phi|}{|\nabla\phi|}\right]. \tag{11}$$

To describe the case of no curvature-driven interface motion [5,6], a local counterterm is introduced into Eq. (11) [26], which gives rise to the local ACE,

$$\phi_t + \mathbf{u}\cdot\nabla\phi = M\Bigg[\nabla^2\phi - \frac{(\nabla\phi\cdot\nabla)|\nabla\phi|}{|\nabla\phi|} - |\nabla\phi|\nabla\cdot\left(\frac{\nabla\phi}{|\nabla\phi|}\right)\Bigg]. \tag{12}$$

With the help of $\nabla\cdot\mathbf{u}=0$ and $|\nabla\phi| = \sqrt{2\beta/k}(\phi_A-\phi)(\phi-\phi_B)$, the conservative and local ACE (12) can be finally written as [5,6]

$$\phi_t + \nabla\cdot(\phi\mathbf{u}) = M\nabla\cdot\left[1-\sqrt{\frac{2\beta}{k}}\frac{(\phi_A-\phi)(\phi-\phi_B)}{|\nabla\phi|}\right]\nabla\phi. \tag{13}$$

C. The hybrid ACE with mass conservation

As pointed out in some previous works [8,9,24], the nonlocal ACE fails to capture small features due to the inherent coarsening process, while for the local ACE, it suffers from numerical dispersion, resulting in the fluctuation of order parameter in the bulk region. In order to reduce the numerical dispersion, Hu *et al.* [8] considered a hybrid ACE for the phase field

$$\frac{\partial\phi}{\partial t} + \nabla\cdot(\phi\mathbf{u}) = M(\nabla^2\phi + D_L + D_N), \tag{14}$$

where the local and nonlocal terms are given by

$$D_L = -\nabla\cdot\lambda\sqrt{\frac{2\beta}{k}}\frac{(\phi_A-\phi)(\phi-\phi_B)}{|\nabla\phi|}\nabla\phi, \tag{15}$$

$$D_N = -(1-\lambda)\frac{4\beta}{\kappa}(\phi-\phi_A)(\phi-\phi_B)\left(\phi-\frac{\phi_A+\phi_B}{2}\right) + \frac{\int_\Omega(1-\lambda)\frac{4\beta}{\kappa}(\phi-\phi_A)(\phi-\phi_B)\left(\phi-\frac{\phi_A+\phi_B}{2}\right)d\mathbf{x}}{\int_\Omega(\phi_A-\phi)(\phi-\phi_B)\,d\mathbf{x}} \times(\phi_A-\phi)(\phi-\phi_B). \tag{16}$$

In Eq. (14) a single global weight λ is used to combine the local AC and nonlocal AC equations. But the coarsening phenomenon cannot be removed since the nonlocal terms still exist partially in the interface region. To settle this problem, we consider a flexible weight λ depending on the phase region,

$$\lambda(\mathbf{x}) = \begin{cases} 0, & \mathbf{x}\in\Omega^{\pm}, \\ 1, & \mathbf{x}\in\Gamma. \end{cases} \tag{17}$$

From above equation, one can find that the local term plays a role only in the interface region $\Gamma(\lambda=1)$, and the advantage of local ACE in capturing small features is remained; at the same time, the nonlocal terms used to reduce the numerical dispersion of order parameter in the bulk region $\Omega^{\pm}$ are also retained. To distinguish the bulk and interface regions, we introduce a signed distance function $\psi(\mathbf{x})$, and Eq. (17) can be rewritten as

$$\lambda(\mathbf{x}) = \begin{cases} 0, & |\psi(\mathbf{x})| \geqslant d_{\min}, \\ 1, & |\psi(\mathbf{x})| < d_{\min}, \end{cases} \tag{18}$$

where $d_{\min}$ is the threshold distance to the interface. In this work the signed distance function $\psi(\mathbf{x})$ is reconstructed by using a predictor-corrector method [27,28]. In the predictor step, $\psi(\mathbf{x})$ is given by

$$\psi(\mathbf{x}) = \begin{cases} -\frac{W}{4}\ln\left(\frac{\phi_A-\phi_B}{\phi-\phi_B}-1\right), \\ -\frac{W}{4}\ln\left(\frac{\phi_A-\phi_B}{\phi_A-0.01-\phi_B}-1\right), \\ -\frac{W}{4}\ln\left(\frac{\phi_A-\phi_B}{\phi_B+0.01-\phi_B}-1\right), \end{cases} \begin{array}{l} (\phi_B+0.01)\leqslant\phi(\mathbf{x})\leqslant(\phi_A-0.01), \\ \phi(\mathbf{x})>(\phi_A-0.01), \\ \phi(\mathbf{x})<(\phi_B+0.01). \end{array} \tag{19}$$

Then a reinitialization equation is solved to correct $\psi(\mathbf{x})$ [27,28]:

$$\partial_{t'}\psi + S(\psi_0)(|\nabla\psi|-1) = 0, \tag{20}$$

where t' is the pseudotime and $\psi_0 = \psi(\mathbf{x}, t'=0) = \psi(\mathbf{x},t)$, and the smeared-out signed function $S(\psi_0)$ is expressed as

$$S(\psi_0) = \frac{\psi_0}{\sqrt{\psi_0^2+\Delta x^2}}. \tag{21}$$

Once the signed distance function $\psi(\mathbf{x})$ is determined, we can get the order parameter through solving the hybrid ACE (14).

D. Navier-Stokes equations

In addition to the above ACEs for phase field, the following Naiver-Stokes equations (NSEs) for incompressible fluid flows are also considered here [18,29]:

$$\nabla\cdot\mathbf{u} = 0, \tag{22a}$$

$$\partial_t(\rho\mathbf{u}) + \nabla\cdot(\rho\mathbf{u}\mathbf{u}) = -\nabla p + \nabla\cdot[\rho\nu(\nabla\mathbf{u}+\nabla\mathbf{u}^T)] + \mathbf{F}_s + \mathbf{G}, \tag{22b}$$

where ρ is density, p is pressure, ν is kinematic viscosity, $\mathbf{F}_s = \mu\nabla\phi$ is surface tension, and $\mathbf{G}$ is body force.

III. NUMERICAL METHOD

A. The MRT-LB model for the improved hybrid ACE

In the past decades, the mesoscopic LB method has gained great success in the study of complex fluid flows and physical systems [10–13]. According to the work of Chai and Shi [30], the evolution equation of MRT-LB model for the improved hybrid ACE can be written as

$$f_j(\mathbf{x}+\mathbf{c}_j\Delta t, t+\Delta t) = f_j(\mathbf{x},t) - \Lambda_{jk}\left[f_k(\mathbf{x},t) - f_k^{eq}(\mathbf{x},t)\right] + \Delta t\left(\delta_{jk}-\frac{\Lambda_{jk}}{2}\right)F_{1k}(\mathbf{x},t) + \Delta t\left[F_{2j}(\mathbf{x},t) + \frac{\Delta t}{2}\partial_t F_{2j}(\mathbf{x},t)\right], \tag{23}$$

where $f_j(\mathbf{x},t)$ is the particle distribution function of order parameter ϕ at position $\mathbf{x}$ and time t, and $f_j^{eq}(\mathbf{x},t)$ is the

equilibrium distribution function. $\mathbf{\Lambda} = \Lambda_{jk}$ is a $q \times q$ invertible collision matrix and can be given by $\mathbf{\Lambda} = \mathbf{M}^{-1}\mathbf{S}_f\mathbf{M}$. Here $\mathbf{S}_f = \mathbf{diag}(s_f^0, s_f^1, s_f^2, \ldots, s_f^{q-1})$ is a diagonal relaxation, and $\mathbf{M}$ is the transformation matrix [17,30]. To correctly recover Eq. (14), the equilibrium distribution function $f_j^{eq}(\mathbf{x}, t)$, the distribution functions of the source terms F_{1j} and F_{2j} should be designed by

$$f_j^{\mathrm{eq}} = \omega_j \phi \left(1 + \frac{\mathbf{c}_j \cdot \mathbf{u}}{c_s^2}\right), \tag{24}$$

$$F_{1j} = \omega_j \frac{\mathbf{c}_j \cdot \left[\partial_t(\phi\mathbf{u}) + c_s^2 \lambda \sqrt{\frac{2\beta}{k}} \frac{(\phi_A - \phi)(\phi - \phi_B)\nabla\phi}{|\nabla\phi|}\right]}{c_s^2},$$

$$F_{2j} = \omega_j M D_N, \tag{25}$$

where ω_j is the weight coefficient, $\mathbf{c}_j$ is the discrete velocity, and c_s is the lattice sound speed. It should be noted that differently from Refs. [8,9], the order parameter can be calculated explicitly by

$$\phi = \sum_j f_j. \tag{26}$$

In addition, it can be shown that the improved hybrid ACE (14) can be recovered correctly with $M_\phi = \Delta t c_s^2(\tau_f - 1/2)$ (see Appendix A).

To compute the time derivative term $\partial_{t'}\psi$ in Eq. (20) and $\partial_t(\phi\mathbf{u})$ in Eq. (25), the first-order Euler method is adopted,

$$\partial_{t'}\psi(\mathbf{x}, t') = [\psi(\mathbf{x}, t') - \psi(\mathbf{x}, t' - \Delta t')]/\Delta t', \tag{27a}$$

$$\partial_t(\phi\mathbf{u})(\mathbf{x}, t) = [(\phi\mathbf{u})(\mathbf{x}, t) - (\phi\mathbf{u})(\mathbf{x}, t - \Delta t)]/\Delta t. \tag{27b}$$

To calculate the gradient and Laplacian terms appeared in the chemical potential and the reinitialization equation, the second-order isotropic central schemes are applied [12,31]:

$$\nabla\chi(\mathbf{x}, t) = \sum_{i\neq 0} \frac{w_i \mathbf{c}_i \chi(\mathbf{x} + \mathbf{c}_i\Delta t, t)}{c_s^2 \Delta t}, \tag{28a}$$

$$\nabla^2\chi(\mathbf{x}, t) = \sum_{i\neq 0} \frac{2w_i \mathbf{c}_i [\chi(\mathbf{x} + \mathbf{c}_i\Delta t, t) - \chi(\mathbf{x}, t)]}{c_s^2 \Delta t^2}. \tag{28b}$$

B. The MRT-LB model for the incompressible NSEs

We now consider the MRT-LB model for the incompressible NSEs (22), and the evolution equation of the model reads [18,19]

$$\begin{aligned} &g_j(\mathbf{x} + \mathbf{c}_j\Delta t, t + \Delta t) \\ &\quad = g_j(\mathbf{x}, t) - (\mathbf{M}^{-1}\mathbf{S}_g\mathbf{M})_{jk}\left[g_k(\mathbf{x}, t) - g_k^{eq}(\mathbf{x}, t)\right] \\ &\qquad + \Delta t[\mathbf{M}^{-1}(\mathbf{I} - \mathbf{S}_g/2)\mathbf{M}]_{jk} G_k(\mathbf{x}, t), \end{aligned} \tag{29}$$

where $g_j(\mathbf{x}, t)$ represents the distribution function for the flow field, $\mathbf{S}_g = \mathbf{diag}(s_g^0, s_g^1, s_g^2, \ldots, s_g^{q-1})$ is the diagonal relaxation matrix, and $g_j^{eq}(\mathbf{x}, t)$ is the equilibrium distribution function and is given by [18]

$$g_j^{\mathrm{eq}} = \begin{cases} \frac{p}{c_s^2}(\omega_j - 1) + \rho s_j(\mathbf{u}), & j = 0, \\ \frac{p}{c_s^2}\omega_j + \rho s_j(\mathbf{u}), & j \neq 0, \end{cases} \tag{30}$$

with

$$s_j(\mathbf{u}) = \omega_j \left[\frac{\mathbf{c}_j \cdot \mathbf{u}}{c_s^2} + \frac{(\mathbf{c}_j \cdot \mathbf{u})^2}{2c_s^4} - \frac{\mathbf{u} \cdot \mathbf{u}}{2c_s^2}\right]. \tag{31}$$

The distribution function of the force term G_j is defined as

$$G_j = \omega_j \left[\mathbf{u} \cdot \nabla\rho + \frac{\mathbf{c}_j \cdot \mathbf{F}}{c_s^2} + \frac{\mathbf{u}\nabla\rho : (\mathbf{c}_j\mathbf{c}_j - c_s^2\mathbf{I})}{c_s^2}\right], \tag{32}$$

where $\mathbf{F} = \mathbf{F}_s + \mathbf{G}$. In addition, the macroscopic velocity and pressure are calculated by

$$\rho\mathbf{u} = \sum_j \mathbf{c}_j g_j + \frac{\Delta t}{2}\mathbf{F}, \tag{33a}$$

$$p = \frac{c_s^2}{1 - \omega_0}\left[\sum_{j\neq 0} g_j + \frac{\Delta t}{2}\mathbf{u} \cdot \nabla\rho + \rho s_0(\mathbf{u})\right]. \tag{33b}$$

With the help of Chapman-Enskog expansion, the incompressible NSEs can be recovered exactly by using $\nu = \Delta t c_s^2(\tau_g - 0.5)$. In the commonly used lattice models, the mesoscopic velocities $\mathbf{c}_j$, the weight coefficients ω_j, and lattice sound speed c_s can be given by the following [32]:

D2Q9:

$$[\mathbf{c}_0, \mathbf{c}_1, \mathbf{c}_2, \mathbf{c}_3, \mathbf{c}_4, \mathbf{c}_5, \mathbf{c}_6, \mathbf{c}_7, \mathbf{c}_8] = \begin{bmatrix} 0 & 1 & 0 & -1 & 0 & 1 & -1 & -1 & 1 \\ 0 & 0 & 1 & 0 & -1 & 1 & 1 & -1 & -1 \end{bmatrix} c,$$

$$\omega_i = \begin{cases} 4/9, & i = 0, \\ 1/9, & i = 1, \ldots, 4, \\ 1/36, & i = 5, \ldots, 8, \end{cases} \quad c_s = c/\sqrt{3}. \tag{34}$$

D3Q7:

$$[\mathbf{c}_0, \mathbf{c}_1, \mathbf{c}_2, \mathbf{c}_3, \mathbf{c}_4, \mathbf{c}_5, \mathbf{c}_6] = \begin{bmatrix} 0 & 1 & 0 & 0 & -1 & 0 & 0 \\ 0 & 0 & 1 & 0 & 0 & -1 & 0 \\ 0 & 0 & 0 & 1 & 0 & 0 & -1 \end{bmatrix} c,$$

$$\omega_i = \begin{cases} 1/8, & i = 0, \\ 1/4, & i = 1, \ldots, 6, \end{cases} \quad c_s = c/2. \tag{35}$$

D3Q15:

$$[\mathbf{c}_0, \mathbf{c}_1, \mathbf{c}_2, \mathbf{c}_3, \mathbf{c}_4, \mathbf{c}_5, \mathbf{c}_6, \mathbf{c}_7, \mathbf{c}_8, \mathbf{c}_9, \mathbf{c}_{10}, \mathbf{c}_{11}, \mathbf{c}_{12}, \mathbf{c}_{13}, \mathbf{c}_{14}]$$
$$= \begin{bmatrix} 0 & 1 & 0 & 0 & -1 & 0 & 0 & 1 & -1 & 1 & 1 & -1 & 1 & -1 & -1 \\ 0 & 0 & 1 & 0 & 0 & -1 & 0 & 1 & 1 & -1 & 1 & -1 & -1 & 1 & -1 \\ 0 & 0 & 0 & 1 & 0 & 0 & -1 & 1 & 1 & 1 & -1 & -1 & -1 & -1 & 1 \end{bmatrix} c,$$
$$\omega_i = \begin{cases} 2/9, & i = 0, \\ 1/9, & i = 1, \ldots, 6, \\ 1/72, & i = 7, \ldots, 14, \end{cases} \quad c_s = c/\sqrt{3}. \tag{36}$$

In this work, we consider the D2Q9 lattice model for both phase and flow fields of two-dimensional problems, while for three-dimensional problems, the D3Q7 and D3Q15 lattice models are used for phase and flow fields, respectively.

IV. NUMERICAL TESTS

In this section, five numerical tests, i.e., the diagonal translation of a circular interface, two stationary bubbles with different radii, a bubble rising under the gravity, the Rayleigh-Taylor instability, and the Plateau-Rayleigh instability, are used to show the capacity of the present LB method in suppressing the numerical dispersion and in capturing small features of two-phase flows. In order to evaluate the numerical dispersion in the bulk region, the largest value of the fluctuation of the order parameter $\delta\phi_{b,\max}$ is adopted:

$$\begin{aligned} \delta\phi_{b,max} &= \max\{a, b\}, \\ a &= \max\{|\phi(\mathbf{x}) - \phi_A|\}, \quad \psi(\mathbf{x}) > d_{\min}, \\ b &= \max\{|\phi(\mathbf{x}) - \phi_B|\}, \quad \psi(\mathbf{x}) < -d_{\min}, \end{aligned} \tag{37}$$

where the threshold distance to the interface $d_{\min}$ is set as $3W$.

A. The diagonal translation of a circular interface

We first consider a simple periodic problem, the diagonal translation of a circular interface, to test the accuracy and convergence of the improved hybrid ACE-LB model. For this problem, a circle with $R = 0.25L_0$ is placed in the center of physical domain $\Omega = (L_0, L_0)$ under a constant velocity $\mathbf{u} = (U_0, U_0)$, and the initial condition of the phase field is given by

$$\phi(x, y, 0) = \frac{\phi_A + \phi_B}{2} + \frac{\phi_A - \phi_B}{2} \times \tanh \frac{2[R - \sqrt{(x - 0.5L_0)^2 + (y - 0.5L_0)^2}]}{W}. \tag{38}$$

Under above conditions, the time interval for the circle returning to the initial center position is $T_0 = L_0/U_0$. In our simulations, the physical parameters are set as $\phi_A = 0.5$, $\phi_B = -0.5$, $L_0 = 128$, $U_0 = 2/L_0$, $M_\phi = 0.01$, $\sigma = 0.001$, $s_f^0 = 1.0$, $s_f^1 = s_f^2 = 1.1$, $s_f^3 = s_f^4 = s_f^5 = s_f^6 = 1/\tau_f$, and $s_f^7 = s_f^8 = 1.0$. To quantitatively measure the accuracy and the convergence of the present ACE-LB model for this time-periodic problem, the relative error of the order parameter ϕ is defined by

$$\mathrm{Err}(\phi) = \sqrt{\frac{\sum_{\mathbf{x}} [\phi(\mathbf{x}, t) - \phi(\mathbf{x}, 0)]^2}{\sum_{\mathbf{x}} \phi(\mathbf{x}, 0)^2}}. \tag{39}$$

First, we present a comparison of different models with different values of interface thickness W for the diagonal motion of a circular interface where the flow field is not considered. From Table I, one can find that considering the relative error $\mathrm{Err}(\phi)$ and the largest value of the fluctuation $\delta\phi_{b,\max}$, the interface thickness $W = 3L_0/64$ for the interface is a good choice in the simulations. Then Fig. 1 depicts a comparison between the present ACE-LB model, the nonlocal ACE-LB model [24], the local ACE-LB model [16], and the hybrid ACE-LB model [8]. As seen from this figure, one can find that the results of the present model at one period, five periods, and ten periods are in good agreement with the initial shape, while the nonlocal model produces a slight deviation. In Table II one

TABLE I. The effect of the interface thickness W on diagonal translation of a circular interface at one period.

W		Present	Nonlocal	Local	Hybrid
$L_0/64$	$\mathrm{Err}(\phi)$	4.9904×10^{-2}	1.4602×10^{-1}	5.0085×10^{-2}	1.8701×10^{-2}
	$\delta\phi_{b,\max}$	2.5964×10^{-4}	2.5860×10^{-4}	8.3240×10^{-4}	2.9287×10^{-4}
$2L_0/64$	$\mathrm{Err}(\phi)$	2.5677×10^{-3}	2.1910×10^{-2}	2.5681×10^{-3}	4.5412×10^{-3}
	$\delta\phi_{b,\max}$	3.7983×10^{-6}	3.8276×10^{-6}	2.5180×10^{-5}	9.0224×10^{-6}
$3L_0/64$	$\mathrm{Err}(\phi)$	1.4117×10^{-3}	7.7310×10^{-3}	1.4119×10^{-3}	2.1068×10^{-3}
	$\delta\phi_{b,\max}$	3.6319×10^{-6}	6.8287×10^{-6}	6.6944×10^{-6}	6.7309×10^{-6}
$4L_0/64$	$\mathrm{Err}(\phi)$	9.6777×10^{-4}	4.2373×10^{-3}	9.6805×10^{-4}	1.3760×10^{-3}
	$\delta\phi_{b,\max}$	4.2862×10^{-6}	8.3453×10^{-6}	8.0565×10^{-6}	8.1116×10^{-6}

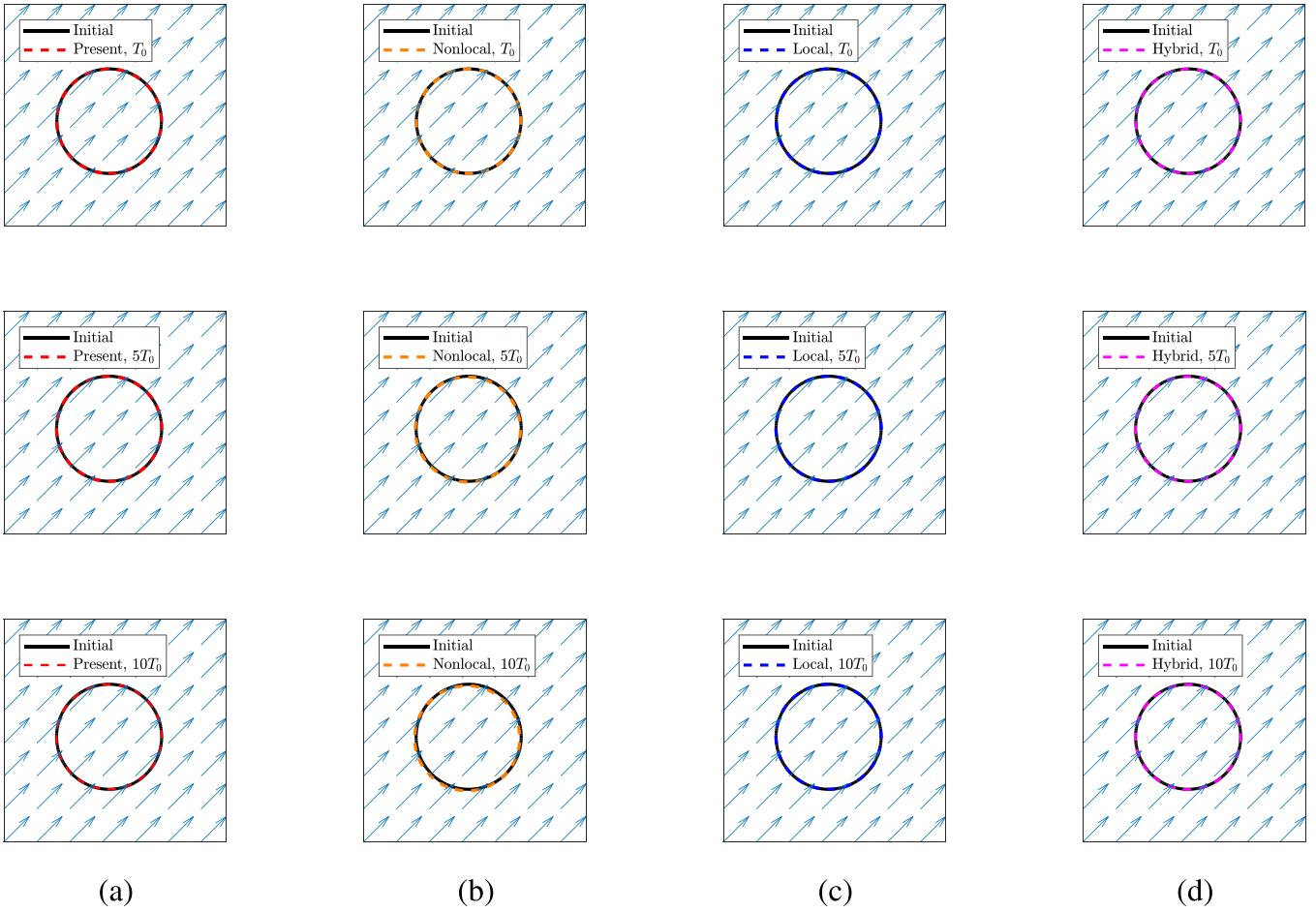

FIG. 1. The phase-field contours ($\phi = 0$) of diagonal motion of a circular interface at $t = 0$ (solid line), $t = T_0$, $t = 5T_0$, and $t = 10T_0$ (dashed line) [(a) the present ACE-LB model, (b) the nonlocal ACE-LB model [24], (c) the local ACE-LB model [16], (d) the hybrid ACE-LB model [8]].

can also observe that the nonlocal and hybrid ACE-LB models have poor performance in capturing the interface, especially after ten periods, while the present model can still work well and give satisfactory results. Besides, the value of $\delta\phi_{b,\max}$ generated by the present model is slightly smaller than those given by other models. Moreover, the present ACE-LB model can also preserve the mass of system. From above comparisons, we can conclude that the present ACE-LB model is more accurate than the nonlocal and hybrid ACE-LB models in capturing the interface and shows a good performance in reducing the numerical dispersion. Finally, this problem is also used to test the convergence rate of the present ACE-LB model in space, and the results shown in Fig. 2 indicate that the present model has a second-order accuracy.

B. Two stationary bubbles with different radii

The classic nonlocal ACE inherently includes the coarsening process such that the smaller bubble eventually disappears when the bubbles with different sizes coexist. We note that this

TABLE II. A comparison of different ACE-LB models for diagonal translation of a circular interface (M_S: mass of system).

		Present	Nonlocal	Local	Hybrid	Initial solution (38)
T_0	$\mathrm{Err}(\phi)$	1.4117×10^{-3}	7.7310×10^{-3}	1.4119×10^{-3}	2.1068×10^{-3}	0
	$\delta\phi_{b,\max}$	3.6319×10^{-6}	6.8287×10^{-6}	6.6944×10^{-6}	6.7309×10^{-6}	0
	M_S	-4.9518×10^{3}	-4.9518×10^{3}	-4.9518×10^{3}	-4.9518×10^{3}	-4.9518×10^{3}
$5T_0$	$\mathrm{Err}(\phi)$	1.5196×10^{-3}	3.5057×10^{-2}	1.5180×10^{-3}	6.1011×10^{-3}	0
	$\delta\phi_{b,\max}$	3.6063×10^{-6}	7.4224×10^{-6}	6.6742×10^{-6}	7.0247×10^{-6}	0
	M_S	-4.9518×10^{3}	-4.9518×10^{3}	-4.9518×10^{3}	-4.9518×10^{3}	-4.9518×10^{3}
$10T_0$	$\mathrm{Err}(\phi)$	1.7187×10^{-3}	6.9631×10^{-2}	1.7135×10^{-3}	1.1644×10^{-2}	0
	$\delta\phi_{b,\max}$	3.6150×10^{-6}	7.0421×10^{-6}	6.6501×10^{-6}	7.1857×10^{-6}	0
	M_S	-4.9518×10^{3}	-4.9518×10^{3}	-4.9518×10^{3}	-4.9518×10^{3}	-4.9518×10^{3}

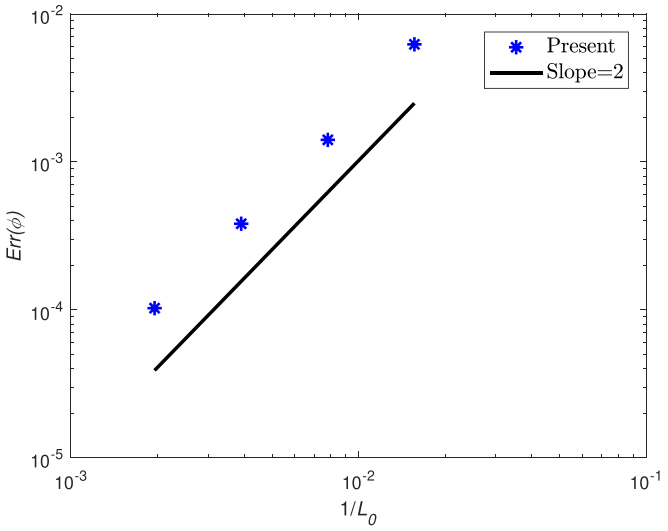

FIG. 2. The convergence rate of the present ACE-LB model in space.

coarsening phenomenon may be undesirable for some two-phase flow problems. Here we take two stationary bubbles with different radii as an example to validate the property of the present LB method in suppressing the coarsening phenomenon. To this end, two bubbles with the radii $R_1 = 0.1L_0$ and $R_2 = 0.15L_0$ are initially placed at a periodic domain $\Omega = (L_0, L_0)$, and the distribution of order parameter ϕ is initialized by

$$\phi(x, y, 0) = \frac{\phi_A + \phi_B}{2} + \frac{\phi_A - \phi_B}{2}\left[\tanh\left(\frac{2\psi_1}{W}\right) + \tanh\left(\frac{2\psi_2}{W}\right) - 1\right], \tag{40}$$

where $\psi_1 = R_1 - \sqrt{(x - 0.25L_0)^2 + (y - 0.25L_0)^2}$ and $\psi_2 = R_2 - \sqrt{(x - 0.57L_0)^2 + (y - 0.57L_0)^2}$. In the following simulations, the physical parameters are set as $\phi_A = 0.5$, $\phi_B = -0.5$, $M_\phi = 1/6$, $\sigma = 0.01$, $\rho_A = 1.0$, $\rho_B = 0.1$, $\nu_A = \nu_B = 0.01$, $L_0 = 300$, $W = 4$, $s_f^0 = 1.0$, $s_f^1 = s_f^2 = 1.1$, $s_f^3 = s_f^4 = s_f^5 = s_f^6 = 1/\tau_f$, $s_f^7 = s_f^8 = 1.2$, $s_g^0 = s_g^3 = s_g^5 = 1.0$, $s_g^1 = s_g^2 = s_g^4 = s_g^6 = 1.1$ and $s_g^7 = s_g^8 = 1/\tau_g$. The simulations are suspended at a sufficiently large number of iterations (about 2.0×10^6), and the interface distributions are plotted at different times in Fig. 3. As seen from this figure, the positions of both bubbles predicted by the present LB method are well maintained. For the nonlocal and hybrid LB methods, however, the smaller bubble gradually shrinks and eventually disappears, while the larger one enlarges with the increase of time. These phenomena also can be observed in Fig. 4(a) where the evolutions of bubble radii in time are presented. Although the results of the local LB method indicate that the radii of both bubbles are approximately conserved during the iterations [see Fig. 4(a)], a large numerical dispersion $\delta\phi_{b,\max}$ inside the bulk phase accelerates the amplification of the artifact owing to the negative feedback by the unexpected surface tension force. Furthermore, both smaller and larger bubbles deviate from the initial position [see Fig. 3(c)]. Additionally, we would also like to point out that $\delta\phi_{b,\max}$ generated by the present LB method almost remains about 10^{-7}, much less than 10^{-3} obtained by the local LB method. These results indicate that the present LB method has a better performance in preserving small features and suppressing the coarsening phenomenon.

C. A bubble rising under the gravity

In this section, a more complicated problem, a rising bubble in water, is also adopted to test the capacity of the present LB method in capturing the large topological changes of interface. The initial setup problem is a stationary gas bubble (B) with diameter D placed in water (A) at (D, D) in computational domain $\Omega = (2D, 4D)$, and the density ratio and viscosity ratio are set to be 1000 and 100, respectively. The periodic boundary condition is applied in the horizontal direction, and the nonslip boundary condition is used on the top and bottom walls. To describe the dynamic behavior of the rising bubble, two dimensionless parameters, the Reynolds number Re and the Eötvös number E_o, are introduced and defined by

$$\mathrm{Re} = \frac{\rho_A U_g D}{\mu_A}, \quad E_o = \frac{\rho_A U_g^2 D}{\sigma}, \tag{41}$$

where $U_g = \sqrt{g_0 D}$, g_0 is the gravitational acceleration, and the characteristic time is $T_0 = tU_g/D$. The initial order

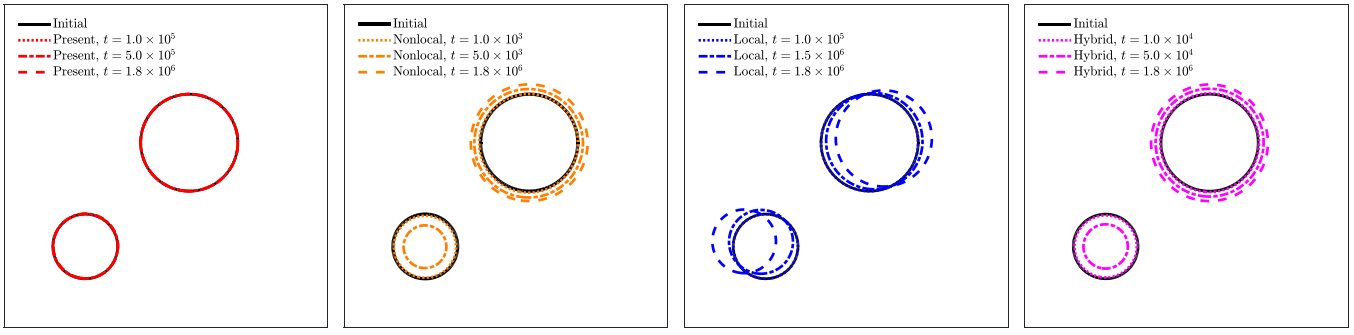

(a) (b) (c) (d)

FIG. 3. The evolutions of phase-field contours ($\phi = 0$) of two stationary bubbles with different radii in time [(a) the present LB method, (b) the nonlocal LB method [24], (c) the local LB method [16], (d) the hybrid LB method [8]].

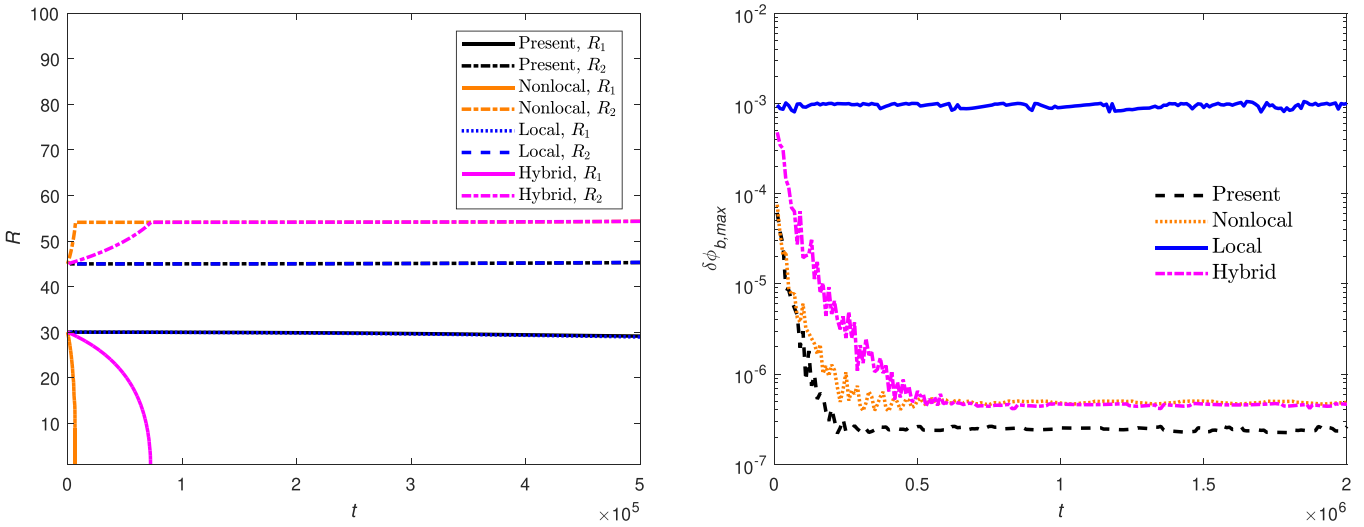

FIG. 4. The evolution process of two bubbles with different radii [(a) the radii of bubbles, (b) the numerical dispersion $\delta\phi_{b,\max}$].

parameter is given by

$$\phi(x,y,0) = \frac{\phi_A+\phi_B}{2} + \frac{\phi_A-\phi_B}{2} \times \tanh\frac{2[\sqrt{(x-D)^2+(y-D)^2}-0.5D]}{W}, \tag{42}$$

and the other parameters are fixed to be $\phi_A = 1.0$, $\phi_B = 0$, $D = 120$, $U_g = 0.005$, $W = 5$, $\rho_A = 100$, $\rho_B = 0.1$, $\mathrm{Re} = 35$, $E_o = 125$, $s_f^0 = 1.0$, $s_f^1 = s_f^2 = 1.2$, $s_f^3 = s_f^4 = s_f^5 = s_f^6 = 1/\tau_f$, $s_f^7 = s_f^8 = 1.2$, $s_g^0 = s_g^3 = s_g^5 = 1.0$, $s_g^1 = s_g^2 = s_g^4 = s_g^6 = 1.1$, and $s_g^7 = s_g^8 = 1/\tau_g$. We perform some simulations and present the evolution of the rising bubble in Fig. 5. As seen from this figure, under the actions of the surface tension and buoyancy forces, the bubble rises and then evolves from the circular shape towards a semicircular shape. As time goes on, a large topological change can be observed that the fluid at the back of the air bubble pushes in and two thin filaments of the bubble are formed. We also make a comparison of the interface shapes predicted by different methods at $t^* = 4.2T_0$ together with the high-accuracy solution of Aland and Viogt [33] in Fig. 6. From this figure, one can see that the nonlocal LB method and hybrid LB method with $\lambda = 0.5$ cannot capture the small features, and to give accurate results, the weight parameter λ of the hybrid LB method should be not less than 0.9 [8]. In contrast, the results of the present LB method are in good agreement with the local LB method and the reported data [33].

Additionally, to give a quantitative comparison, we also measure the vertical position of the mass center of the bubble Y_c and the numerical dispersion $\delta\phi_{b,\max}$ during the bubble

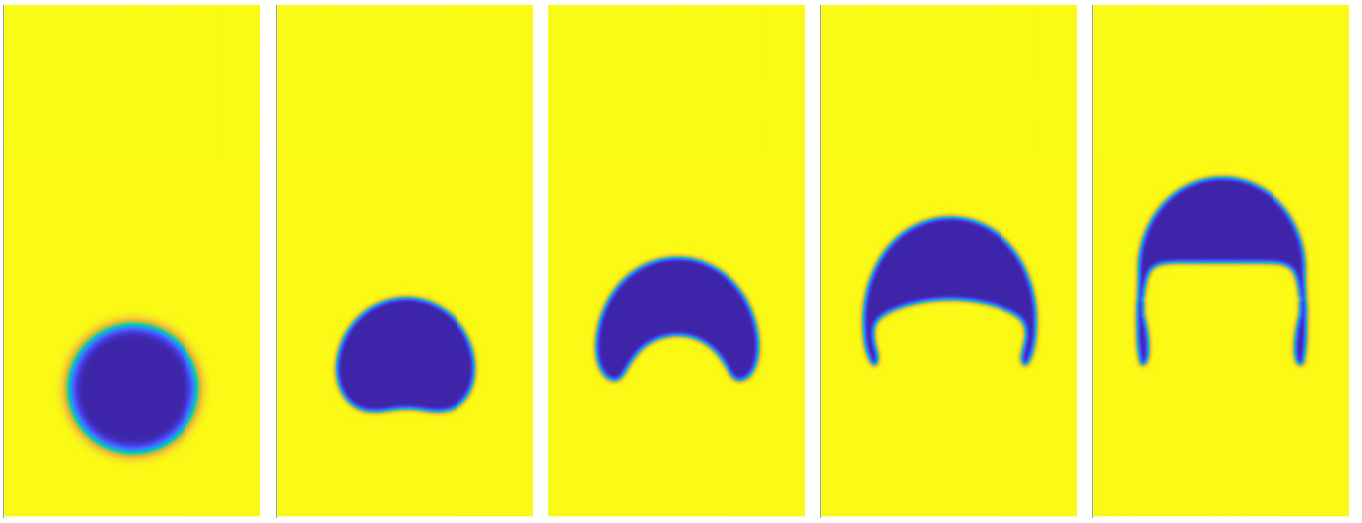

FIG. 5. Evolution of bubble shape in time [(a) $t^* = 0$, (b) $t^* = T_0$, (c) $t^* = 2T_0$, (d) $t^* = 3T_0$, (e) $t^* = 4T_0$].

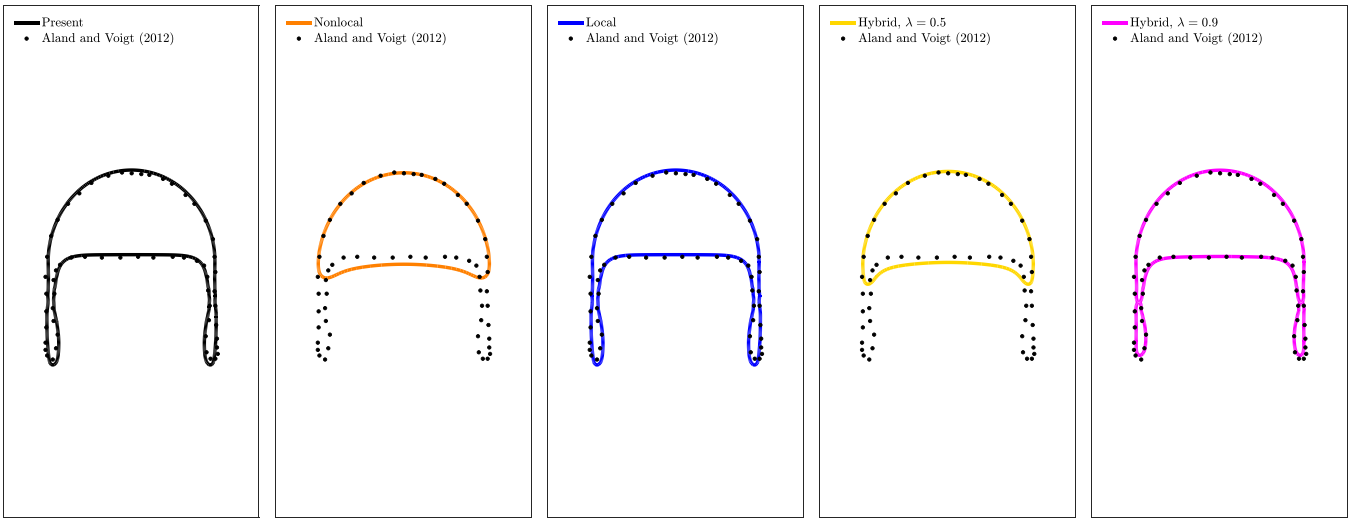

FIG. 6. A comparison of some different methods in predicting the interface shape of the bubble rising at $t^* = 4.2T_0$ [(a) the present LB method, (b) the nonlocal LB method [24], (c) the local LB method [16], (d) the hybrid LB method with $\lambda = 0.5$ [8], (e) the hybrid LB method with $\lambda = 0.9$ [8]].

rising process. Mathematically, the mass center of the bubble Y_c can be calculated by

$$Y_c = \frac{\sum_{i,j} y_j H_d[5(0.5-\phi)]}{\sum_{i,j} H_d[5(0.5-\phi)]}, \tag{43}$$

with H_d being the smeared-out Heaviside function

$$H_d(x) = \begin{cases} 0, & x < -2, \\ 0.5 + 0.25x + \frac{0.5}{\pi}\sin(0.5\pi x), & -2 \leqslant x \leqslant 2, \\ 1, & x > 2. \end{cases} \tag{44}$$

We conduct some simulations with different methods and plot the results in Fig. 7. As shown in this figure, although these methods can give the satisfactory results in predicting the mass center Y_c, the numerical dispersion $\delta\phi_{b,\max}$ generated by the present method has the smallest amplitude oscillation. The results also illustrate that compared to the commonly used local LB method, the present method can reduce at least one order of magnitude of the order parameter fluctuation.

D. The Rayleigh-Taylor instability

To further demonstrate the accuracy of the present method for more complicated flows, the classic Rayleigh-Taylor instability is also investigated, which takes place when a heavy

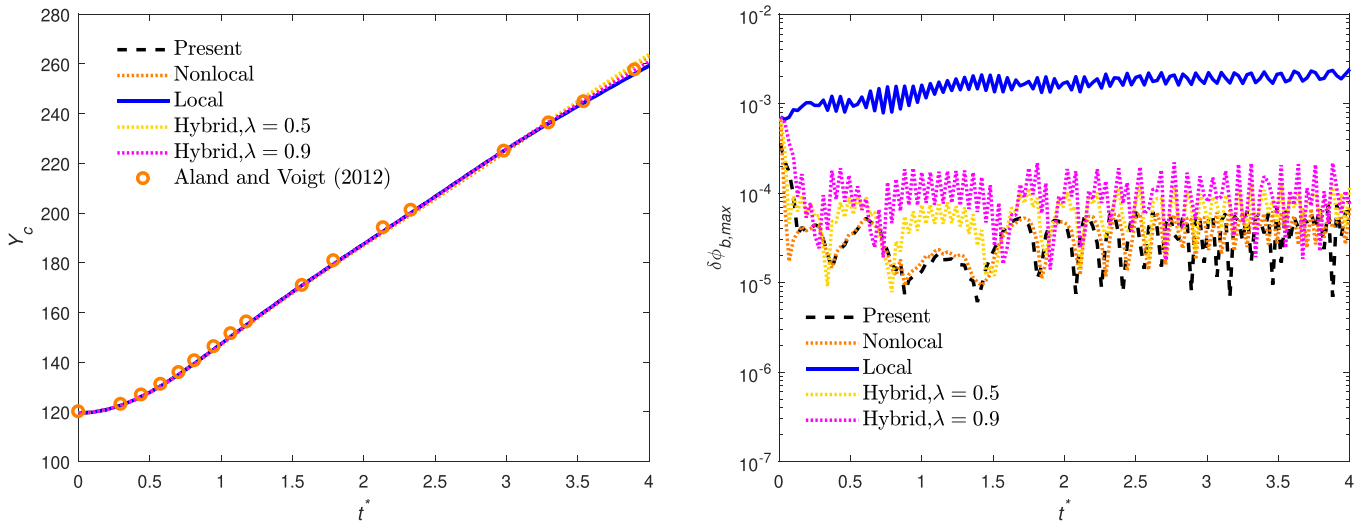

FIG. 7. The comparisons of some different methods for the bubble rising problem with $\mathrm{Re} = 35$ and $E_o = 125$ [(a) the mass center of bubble Y_c, (b) the numerical dispersion $\delta\phi_{b,\max}$].

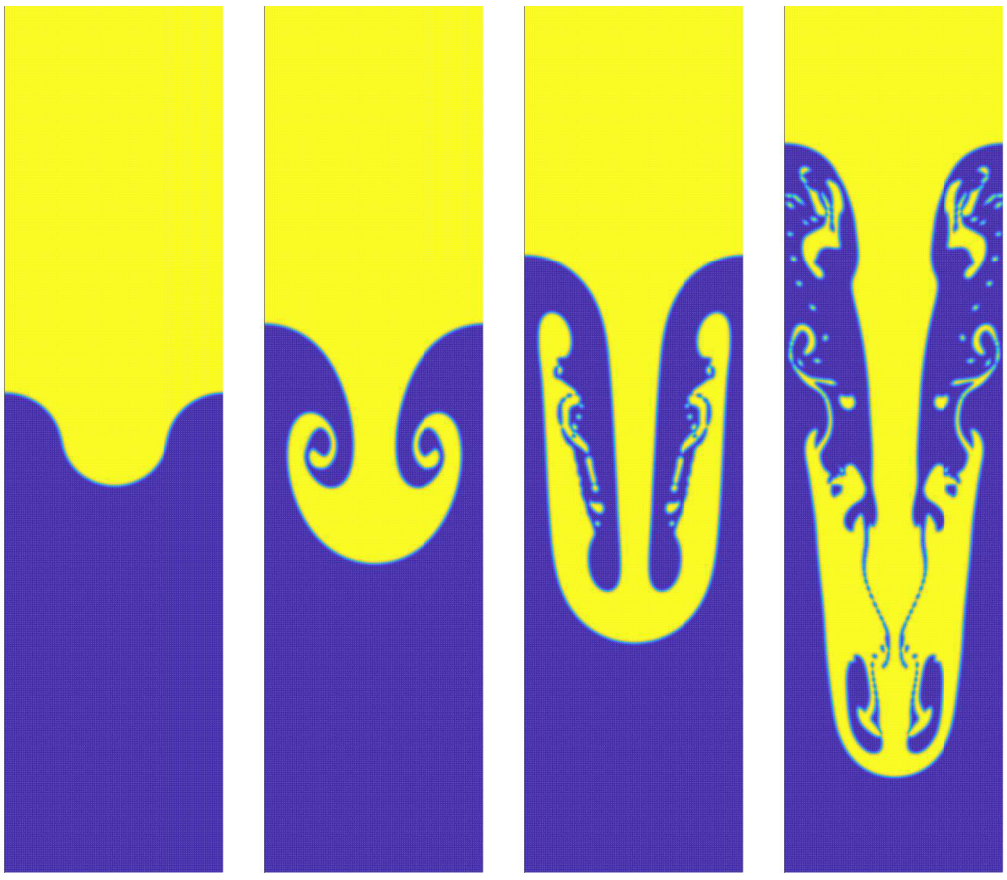

FIG. 8. Evolution of the interface pattern of the two-dimensional Rayleigh-Taylor instability [(a) $t^* = T_0$, (b) $t^* = 2T_0$, (c) $t^* = 3T_0$, (d) $t^* = 4T_0$].

fluid A rests on top of a light fluid B with an initial perturbation at the interface. We first consider a two-dimensional Rayleigh-Taylor instability in a rectangular computational domain $[0, d] \times [0, 4d]$ with periodic boundary condition on the left and right sides and no-slip condition on the top and bottom walls. Initially, the profile of the order parameter is set as

$$\phi(x, y, 0) = \frac{\phi_A + \phi_B}{2} + \frac{\phi_A - \phi_B}{2} \tanh \frac{2(y - h)}{W}, \quad (45)$$

where $h = 2d + 0.05d \cos(2\pi x/d)$. In order to characterize the Rayleigh-Taylor instability problem, the dimensionless Reynolds number Re, the Atwood number At, and the Péclet number Pe are defined, respectively, as

$$\mathrm{Re} = \frac{d}{v}\sqrt{\frac{At\,gd}{1 + At}}, \quad At = \frac{\rho_A - \rho_B}{\rho_A + \rho_B}, \quad \mathrm{Pe} = \frac{d\sqrt{gd}}{M_\phi}, \quad (46)$$

where g is a gravitational acceleration and the normalized time is defined by $t^* = t\sqrt{At\,g/d}$. The other simulation parameters are chosen as $\phi_A = 1.0$, $\phi_B = -1.0$, $d = 256$, $\sqrt{gd} = 0.04$, $\sigma = 5.0 \times 10^{-5}$, $\mathrm{Re} = 3000$, $\mathrm{At} = 0.1$, $\mathrm{Pe} = 1000$, $\rho_B = 1$, $s_f^0 = 1.0$, $s_f^1 = s_f^2 = 1.2$, $s_f^3 = s_f^4 = s_f^5 = s_f^6 = 1/\tau_f$, $s_f^7 = s_f^8 = 1.2$, $s_g^0 = s_g^1 = s_g^2 = s_g^3 = s_g^5 = 1.0$, $s_g^4 = s_g^6 = 1.7$ and $s_g^7 = s_g^8 = 1/\tau_g$. At the early stage, the heavy (yellow) fluid forms a spike shape from its initial convex shape and rolls up into two counterrotating vortices along the sides of the spike [see Fig. 8(b)]. With the increase of time, the interface undergoes a chaotic breakup, which results in a large number of small dissociative droplets in the system [see Figs. 8(c) and 8(d)]. We also show the interface pattern of the two-dimensional Rayleigh-Taylor instability among different methods in Fig. 9, where $t^* = 4T_0$. From this figure, one can find that the result of present method is close to that obtained by the local LB method, but these small dissociative droplets cannot be captured in detail by using the nonlocal and hybrid LB methods.

To give a quantitative comparison of different methods, the positions of the bubble front and spike tip are plotted in Fig. 10(a). The results show good quantitative agreement among them, except for a minor discrepancy caused by the nonlocal LB method. In addition, the numerical dispersion $\delta\phi_{b,\max}$ has also been considered in Fig. 10(b), and one can find that $\delta\phi_{b,\max}$ obtained by the local LB method is larger than 10^{-3}, but it is smaller than 10^{-4} when the present method is adopted. Moreover, the result of the hybrid LB method has a large oscillation in the chaotic stage, which indicates that a global weight λ fails to suppress the numerical dispersion for complex two-phase flows.

Next, the three-dimensional Rayleigh-Taylor instability is also used to test the present LB method for more complicated flows. In a rectangular box with $[0, d] \times [0, d] \times$

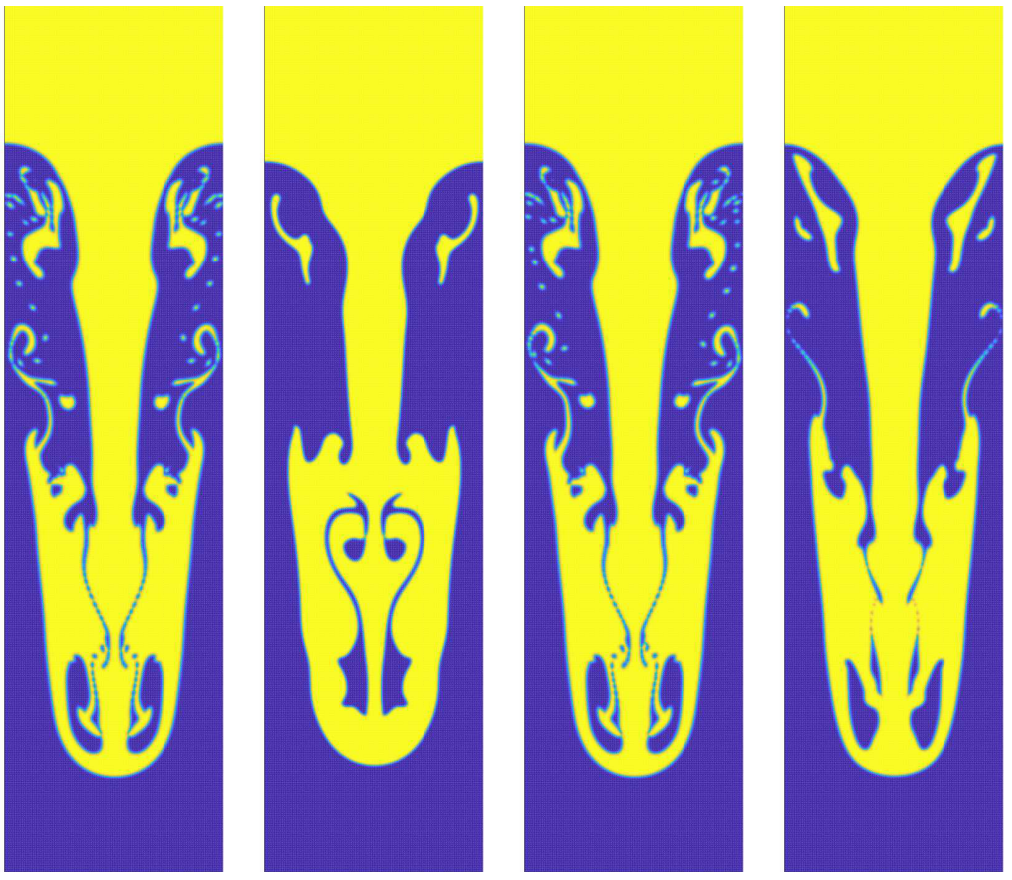

(a) (b) (c) (d)

FIG. 9. A comparison of some different methods for the interface patterns of the two-dimensional Rayleigh-Taylor instability at $t^* = 4T_0$ [(a) the present LB method, (b) the nonlocal LB method [24], (c) the local LB method [16], (d) the hybrid LB method [8]].

$[0, 4d]$, the initial position of the interface is set by $h = 0.05d[\cos(2\pi x/d) + \cos(2\pi y/d)]$. To be consistent with the previous study [34], the Reynolds number is chosen as $\mathrm{Re} = d^{3/2}g^{1/2}/\nu = 128$, the capillary number $\mathrm{Ca} = \mu_A\sqrt{gd}/\sigma = 960$, $t^* = t/\sqrt{d/g}$, and other parameters are fixed to be $\phi_A = 1$, $\phi_B = 0$, $d = 64$, $\sqrt{gd} = 0.04$, $\mathrm{At} = 0.5$, $\mathrm{Pe} = 1024$,

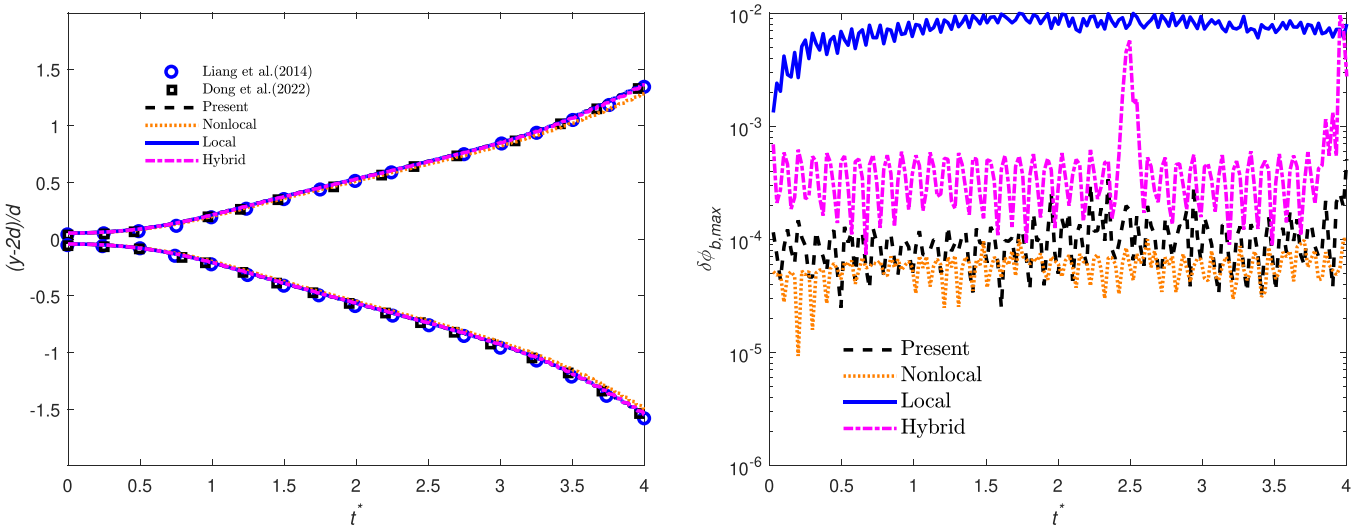

FIG. 10. The comparisons of some different methods for the two-dimensional Rayleigh-Taylor instability [(a) the positions of the bubble front and spike tip, (b) the numerical dispersion $\delta\phi_{b,\max}$].

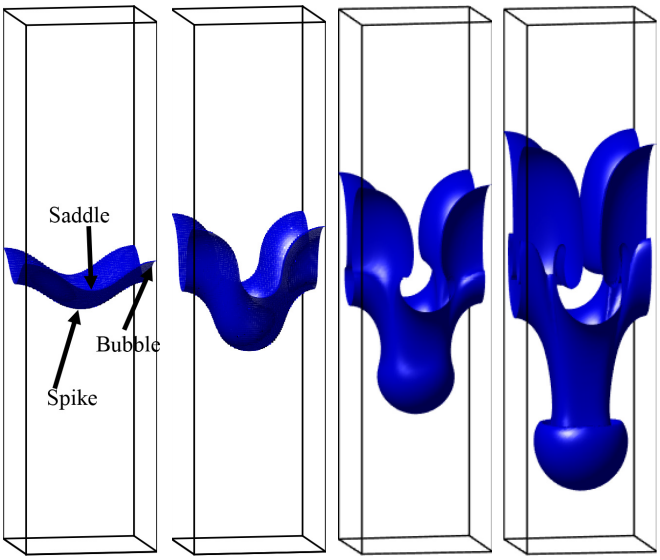

FIG. 11. Evolution of the interface pattern of the three-dimensional Rayleigh-Taylor instability [(a) $t^* = T_0$, (b) $t^* = 2T_0$, (c) $t^* = 3T_0$, (d) $t^* = 4T_0$].

$W = 5$, $\rho_A = 1$, $s_f^0 = s_f^4 = s_f^5 = s_f^6 = 1.0$, $s_f^1 = s_f^2 = s_f^3 = 1/\tau_f$, $s_g^0 = s_g^1 = s_g^2 = s_g^3 = s_g^{10} = s_g^{11} = s_g^{12} = s_g^{13} = 1.0$ and $s_g^4 = s_g^5 = s_g^6 = s_g^7 = s_g^8 = s_g^9 = s_g^{14} = 1/\tau_g$. Under the influence of gravity, the heavy and light fluids penetrate into each other to form the spike and bubble. Meanwhile, four saddle points are formed at the middle of the four sides of the rectangular box. We also consider the spike tip, saddle point, and bubble front [see Fig. 11(a)] and carry out a comparison between the present method and the available data [34] in Fig. 12. As seen from this figure, there is a good agreement between them, which also demonstrates that the present method can be used to deal with the three-dimensional two-phase flows.

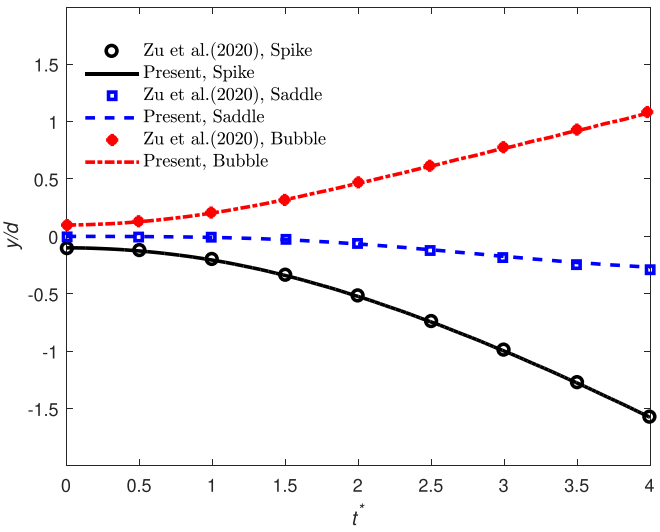

FIG. 12. A comparison between the present method and the previous work [34] for the positions of the bubble front, saddle point and spike tip in the three-dimensional Rayleigh-Taylor instability.

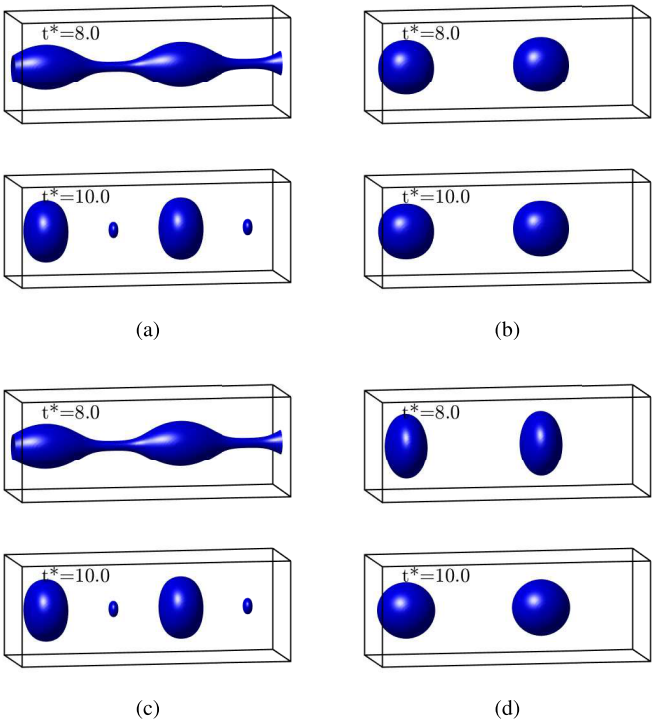

FIG. 13. A comparison of some different methods for the interface patterns of the three-dimensional Plateau-Rayleigh instability at $t^* = 8$ and $t^* = 10$ [(a) the present LB method, (b) the nonlocal LB method [24], (c) the local LB method [16], (d) the hybrid LB method [8]].

E. The three-dimensional Plateau-Rayleigh instability

To show the potential of the present LB method in the study of the three-dimensional complex flows, the Plateau-Rayleigh instability that causes the breakup of a liquid ligament into smaller droplets is studied in this section. The simulations are carried out in a domain $[0, 8d] \times [0, 3d] \times [0, 3d]$ with periodic boundary condition, and the initial order profile is set to be

$$\phi(x, y, z, 0) = \frac{\phi_A + \phi_B}{2} + \frac{\phi_A - \phi_B}{2} \times \tanh \frac{2[r(x) - \sqrt{(z - 1.5d)^2 + (y - 1.5d)^2}]}{W}, \tag{47}$$

where $r(x) = R_0 + \delta \sin(\pi x/2d)$, R_0 is the unperturbed ligament radius, and δ is the perturbation. In order to characterize the Plateau-Rayleigh instability, the Ohnesorge number Oh and the capillary time t_{cap} are defined as

$$\text{Oh} = \frac{\mu_A}{\sqrt{\rho_A \sigma R_0}}, \quad t_{\text{cap}} = \sqrt{\frac{\rho_A R_0^3}{\sigma}}. \tag{48}$$

The other simulation parameters are set as $\phi_A = 1.0$, $\phi_B = 0$, $M = 0.5$, $W = 3$, $\rho_A = 2.1$, $\rho_B = 0.078$, $d = 32$, $R_0 = 14$, $\text{Oh} = 0.1$, $t_{\text{cap}} = 800$, $s_f^0 = 1.0$, $s_f^4 = s_f^5 = s_f^6 = 1.2$, $s_f^1 = s_f^2 = s_f^3 = 1/\tau_f$, $s_g^0 = s_g^1 = s_g^2 = s_g^3 = s_g^{10} = s_g^{11} = s_g^{12} = s_g^{13} = 1.0$, and $s_g^4 = s_g^5 = s_g^6 = s_g^7 = s_g^8 = s_g^9 = s_g^{14} = 1/\tau_g$. For the case of $\text{Oh} = 0.1$, the liquid ligament first

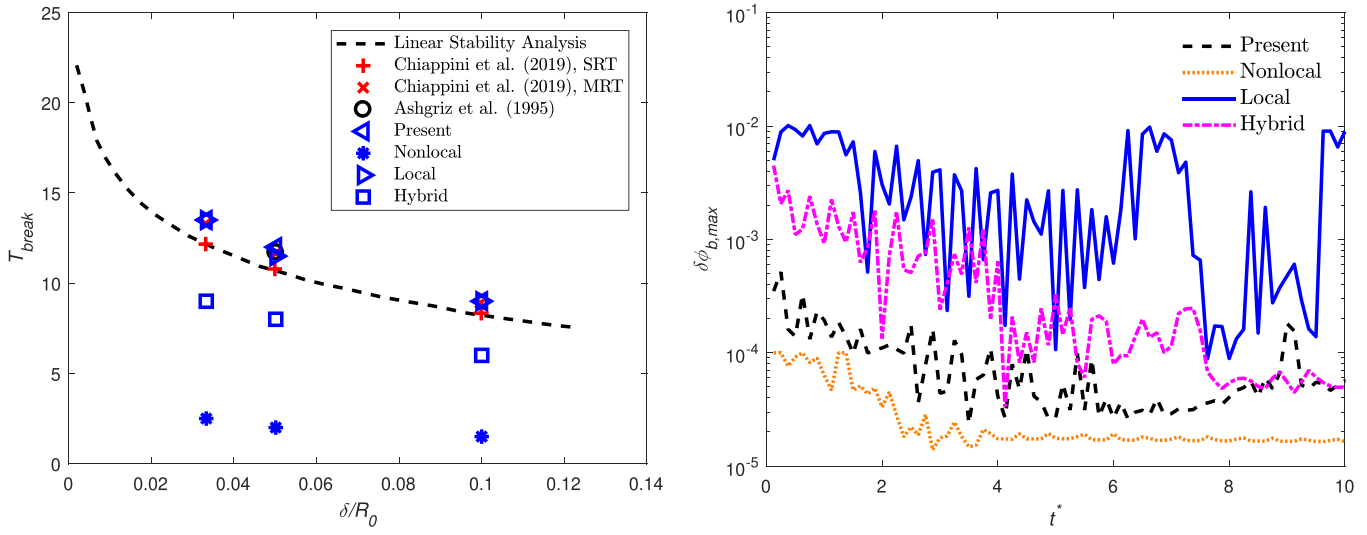

(a) (b)

FIG. 14. The comparisons of some different methods for the three-dimensional Plateau-Rayleigh instability [(a) the influence of the initial perturbation on the nondimensional breakup time, (b) the numerical dispersion $\delta\phi_{b,\max}$].

begins to contract and then breaks into two mother droplets and two satellite droplets [see Figs. 13(a) and 13(c)]. However, the satellite droplets still cannot be captured by using the nonlocal and hybrid LB methods. To give a quantitative comparison of different methods, the influence of the initial perturbation δ/R_0 on the nondimensional breakup time are plotted in Fig. 14(a). One can be found that the present and local LB methods are well aligned with some available data [35,36], whereas it takes less time for the liquid ligament to break up by using the nonlocal or hybrid LB method. In addition, the numerical dispersion $\delta\phi_{b,\max}$ has also been shown in Fig. 14(b), and the results show that $\delta\phi_{b,\max}$ obtained by the local LB method is larger than that obtained by the present method.

V. CONCLUSIONS

In this paper, we developed a conservative phase-field LB method for incompressible two-phase flow where a hybrid ACE with a flexible weight for the phase field is performed. Then we conducted comparative studies of the present method, the local method, the nonlocal method, and the hybrid method for the two-phase flow in reducing the numerical dispersion and the coarsening phenomenon, and the numerical results show that the present LB method produces better performance in capturing small features than the nonlocal and hybrid methods; besides, it can be reduced almost one order of magnitude of the order parameter fluctuation than the local method. Finally, considering the above advantages of the present method in depicting an incompressible two-phase flow, the present LB method could be developed as an effective tool for multiphase flows in a future work.

ACKNOWLEDGMENTS

The computation is completed in the HPC Platform of Huazhong University of Science and Technology. This work is financially supported by the National Natural Science Foundation of China (Grants No. 12072127 and No. 51836003) and the Fundamental Research Funds for the Central Universities, HUST (No. 2021JYCXJJ010).

APPENDIX A: THE CHAPMAN-ENSKOG ANALYSIS OF THE LB MODEL FOR THE HYBRID AC EQUATION

We first perform a Chapman-Enskog analysis in which f_j, F_{1j}, F_{2j}, ∂_t, and ∇ are expanded as

$$\begin{aligned} f_j &= f_j^{(0)} + \epsilon f_j^{(1)} + \epsilon^2 f_j^{(2)}, \\ F_{1j} &= \epsilon F_{1j}^{(1)} + \epsilon^2 F_{1j}^{(2)}, \quad F_{2j} = \epsilon F_{2j}^{(1)} + \epsilon^2 F_{2j}^{(2)}, \\ \partial_t &= \epsilon\partial_{t_1} + \epsilon^2\partial_{t_2}, \quad \nabla = \epsilon\nabla_1, \end{aligned} \tag{A1}$$

where ϵ is a small parameter. Applying the Taylor expansion to Eq. (23), we have

$$\begin{aligned} &D_j f_j + \frac{\Delta t}{2} D_j^2 f_j + \cdots \\ &\quad = -\frac{1}{\Delta t}\Lambda_{jk} f_k^{\mathrm{ne}} + \left(\delta_{jk} - \frac{\Lambda_{jk}}{2}\right) F_{1k}(\mathbf{x},t) + F_{2j}(\mathbf{x},t) \\ &\qquad + \frac{\Delta t}{2}\partial_t F_{2j}(\mathbf{x},t), \end{aligned} \tag{A2}$$

where $D_j = \partial_t + \mathbf{c}_j \cdot \nabla$. Substituting Eq. (A1) into Eq. (A2) yields the following equations at different orders of ϵ:

$$\epsilon^0 : \Lambda_{jk}\left(f_k^{(0)} - f_k^{\mathrm{eq}}\right) = 0, \tag{A3a}$$

$$\begin{aligned} &\epsilon^1 : D_{1j} f_j^{(0)} \\ &\quad = -\frac{1}{\Delta t}\Lambda_{jk} f_k^{(1)} + \left(\delta_{jk} - \frac{\Lambda_{jk}}{2}\right) F_{1k}^{(1)}(\mathbf{x},t) + F_{2j}^{(1)}(\mathbf{x},t), \end{aligned} \tag{A3b}$$

$$\epsilon^2 : \partial_{t_2} f_j^{(0)} + D_{1j} f_j^{(1)} + \frac{\Delta t}{2} D_{1j}^2 f_j^{(0)}$$
$$= -\frac{1}{\Delta t}\mathbf{\Lambda}_{jk} f_k^{(2)} + \left(\delta_{jk} - \frac{\Lambda_{jk}}{2}\right) F_{1k}^{(2)}(\mathbf{x}, t) + F_{2j}^{(2)}(\mathbf{x}, t)$$
$$+ \frac{\Delta t}{2}\partial_{t_1} F_{2j}^{(1)}(\mathbf{x}, t), \tag{A3c}$$

where $D_{1j} = \partial_{t_1} + \mathbf{c}_j \cdot \nabla_1$. With the help of Eq. (A3b), we can rewrite Eq. (A3c) as

$$\partial_{t_2} f_j^{(0)} + D_{1j}\left(\delta_{jk} - \frac{\mathbf{\Lambda}_{jk}}{2}\right)\left(f_k^{(1)} + \frac{\Delta t}{2} F_{1k}^{(1)}\right) + \frac{\Delta t}{2} D_{1j} F_{2j}^{(1)}$$
$$= -\frac{1}{\Delta t}\mathbf{\Lambda}_{jk} f_k^{(2)} + \left(\delta_{jk} - \frac{\Lambda_{jk}}{2}\right) F_{1k}^{(2)}(\mathbf{x}, t) + F_{2j}^{(2)}(\mathbf{x}, t)$$
$$+ \frac{\Delta t}{2}\partial_{t_1} F_{2j}^{(1)}(\mathbf{x}, t). \tag{A4}$$

In addition, one can also obtain that the equilibrium distribution function and discrete source terms satisfy the following moment conditions:

$$\sum_i \mathbf{e}_i \Lambda_{ij} = s_0 \mathbf{e}_j, \quad \sum_i \mathbf{c}_i \Lambda_{ij} = s_1 \mathbf{c}_j, \quad \sum_j f_j^{eq} = \phi,$$
$$\sum_j \mathbf{c}_j f_j^{eq} = \phi \mathbf{u}, \quad \sum_j \mathbf{c}_j \mathbf{c}_j f_j^{eq} = c_s^2 \phi \mathbf{I}, \quad \sum_j F_{1j} = 0,$$
$$\sum_j \mathbf{c}_j F_{1j} = \partial_t(\phi \mathbf{u}) + c_s^2 \lambda \sqrt{\frac{2\beta}{k}} \frac{(\phi_A - \phi)(\phi - \phi_B)\nabla\phi}{|\nabla\phi|},$$
$$\sum_j F_{2j} = M D_N, \quad \sum_j \mathbf{c}_j F_{2j} = 0. \tag{A5}$$

With the help of above equation and summing Eqs. (A3b) and (A4) over j, we have

$$\partial_{t_1}\phi + \nabla_1 \cdot (\phi \mathbf{u}) = M D_N^{(1)}, \tag{A6}$$

$$\partial_{t_2}\phi + \nabla_1 \cdot \left(1 - \frac{1}{2\tau_f}\right)\left\{\sum_k \mathbf{c}_k f_k^{(1)} + \frac{\Delta t}{2}\left[\partial_{t_1}(\phi \mathbf{u}) + c_s^2 \lambda \sqrt{\frac{2\beta}{k}} \frac{(\phi_A - \phi)(\phi - \phi_B)\nabla_1\phi}{|\nabla\phi|}\right]\right\}$$
$$= M D_N^{(2)}, \tag{A7}$$

where $M D_N = \epsilon M D_N^{(1)} + \epsilon^2 M D_N^{(2)}$. Based on Eq. (A3b), we can also derive the first-order moment of $f_j^{(1)}$,

$$\sum_j \mathbf{c}_j f_j^{(1)} = -\Delta t \tau_f \left[\nabla_1 \cdot c_s^2 \phi \mathbf{I} + \frac{1}{2\tau_f}\partial_{t_1}(\phi \mathbf{u}) - \left(1 - \frac{1}{2\tau_f}\right) c_s^2 \lambda \sqrt{\frac{2\beta}{k}} \frac{(\phi_A - \phi)(\phi - \phi_B)\nabla_1\phi}{|\nabla\phi|}\right]. \tag{A8}$$

Substituting Eq. (A8) into Eq. (A7), one can get

$$\partial_{t_2}\phi = \nabla_1 \cdot \Delta t c_s^2 \left(\tau_f - \frac{1}{2}\right) \times \left[\nabla_1\phi - \lambda \sqrt{\frac{2\beta}{k}} \frac{(\phi_A - \phi)(\phi - \phi_B)\nabla_1\phi}{|\nabla\phi|}\right] + M D_N^{(2)}. \tag{A9}$$

Then combining Eqs. (A6) and (A9) and taking $M = \Delta t c_s^2(\tau_f - 1/2)$, one can correctly recover the hybrid ACE (14).

APPENDIX B: THE STATIC DROPLET

In this Appendix the static droplet is used to verify the present LB method. A liquid droplet with the radius $R = 50$ is located at the center of the domain $[0, 4R] \times [0, 4R]$ with the

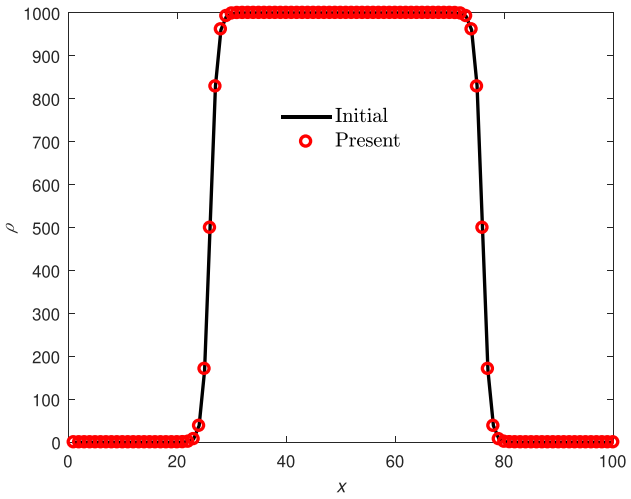

(a)

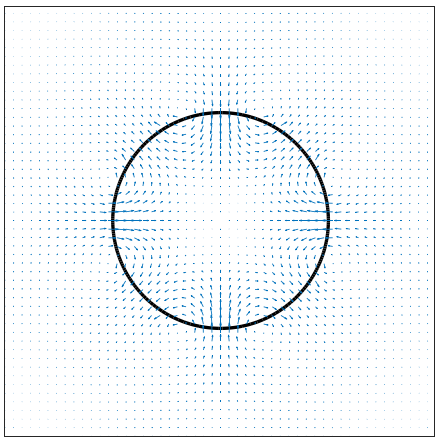

(b)

FIG. 15. (a) The density distribution along the horizonal center line, (b) the velocity distribution of the whole domain at the equilibrium state with $|\mathbf{u}|_{\max} = 4.26 \times 10^{-9}$.

periodic boundary condition. The order profile is initialized by

$$\phi(x, y, 0) = \frac{\phi_A + \phi_B}{2} + \frac{\phi_A - \phi_B}{2} \times \tanh \frac{2[R - \sqrt{(x - 2R)^2 + (y - 2R)^2}]}{W}. \quad \text{(B1)}$$

In the simulation, the other parameters are set as $\phi_A = 1$, $\phi_B = 0$, $\rho_A = 1000$, $\rho_B = 1$, $\nu_A = 0.1$, $\nu_B = 0.1$, $\sigma = 0.001$, and $W = 5$. Figure 15(a) shows that the density distribution of the droplet at the equilibrium with the initial one. It is found that they are close to each other. As seen in Fig. 15(b), one can observe that the spurious velocities indeed exist around the interface, and their maximum magnitude computed by $|\mathbf{u}|_{\max} = \sqrt{u^2 + v^2}_{\max}$ has an order of 10^{-9}.

[1] D. Anderson, G. McFadden, and A. Wheeler, Diffuse-interface methods in fluid mechanics, Annu. Rev. Fluid Mech. **30**, 139 (1998).

[2] J. Cahn and J. Hilliard, Free energy of a non-uniform system I: Interfacial free energy, J. Chem. Phys. **28**, 258 (1958).

[3] S. Allen and J. Cahn, Mechanisms of phase transformations within the miscibility gap of Fe-rich Fe-Al alloys, Acta Metall. **24**, 425 (1976).

[4] J. Rubinstein and P. Sternberg, Nonlocal reaction-diffusion equations and nucleation, IMA J. Appl. Math. **48**, 249 (1992).

[5] Y. Sun and C. Beckermann, Sharp interface tracking using the phase-field equation, J. Comput. Phys. **220**, 626 (2007).

[6] P. Chiu and Y. Lin, A conservative phase field method for solving incompressible two-phase flows, J. Comput. Phys. **230**, 185 (2011).

[7] F. Ren, B. Song, M. Sukop, and H. Hu, Improved lattice Boltzmann modeling of binary flow based on the conservative Allen-Cahn equation, Phys. Rev. E **94**, 023311 (2016).

[8] Y. Hu, D. Li, and L. Jin, Hybrid Allen-Cahn-based lattice Boltzmann model for incompressible two-phase flows: The reduction of numerical dispersion, Phys. Rev. E **99**, 023302 (2019).

[9] D. Kang and T. Yun, Local hybrid Allen-Cahn model in phase-field lattice Boltzmann method for incompressible two-phase flow, Phys. Rev. E **105**, 045307 (2022).

[10] S. Chen and G. Doolen, Lattice Boltzmann method for fluid flows, Annu. Rev. Fluid Mech. **30**, 329 (1998).

[11] S. Succi, *The Lattice Boltzmann Equation for Fluid Dynamics and Beyond* (Oxford University Press, Oxford, 2001).

[12] Z. Guo and C. Shu, *Lattice Boltzmann Method and Its Applications in Engineering* (World Scientific, Singapore, 2013).

[13] T. Krüger, H. Kusumaatmaja, A. Kuzmin, O. Shardt, G. Silva, and E. Viggen, *The Lattice Boltzmann Method: Principles and Practice* (Springer, Cham, Switzerland, 2017).

[14] A. Facci, M. Lauricella, S. Succi, V. Villani, and G. Falcucci, Optimized modeling and design of a PCM-enhanced H_2 storage, Energies **14**, 1554 (2021).

[15] G. Falcucci, G. Amati, P. Fanelli, K. Krastev, G. Polverino, M. Porfiri, and S. Succi, Extreme flow simulations reveal skeletal adaptations of deep-sea sponges, Nature London **595**, 537 (2021).

[16] H. Wang, Z. Chai, B. Shi, and H. Liang, Comparative study of the lattice Boltzmann models for Allen-Cahn and Cahn-Hilliard equations, Phys. Rev. E **94**, 033304 (2016).

[17] H. Liang, B. Shi, Z. Guo, and Z. Chai, Phase-field-based multiple-relaxation-time lattice Boltzmann model for incompressible multiphase flows, Phys. Rev. E **89**, 053320 (2014).

[18] H. Liang, J. Xu, J. Chen, H. Wang, Z. Chai, and B. Shi, Phase-field-based lattice Boltzmann modeling of large-density-ratio two-phase flows, Phys. Rev. E **97**, 033309 (2018).

[19] X. Liu, Z. Chai, and B. Shi, Phase-field-based axisymmetric lattice Boltzmann method for two-phase electro-hydrodynamic flows, Commun. Comput. Phys. **30**, 1346 (2021).

[20] X. Liu, Z. Chai, C. Zhan, B. Shi, and W. Zhang, A diffuse-domain phase-field based lattice Boltzmann method for two-phase flows in complex geometries, Multiscale Model. Simul. **20**, 1411 (2022).

[21] A. Fakhari and M. Rahimian, Phase-field modeling by the method of lattice Boltzmann equations, Phys. Rev. E **81**, 036707 (2010).

[22] Y. Zu and S. He, Phase-field-based lattice Boltzmann model for incompressible binary fluid systems with density and viscosity contrasts, Phys. Rev. E **87**, 043301 (2013).

[23] M. Geier, A. Fakhari, and T. Lee, Conservative phase-field lattice Boltzmann model for interface tracking equation, Phys. Rev. E **91**, 063309 (2015).

[24] Z. Chai, D. Sun, H. Wang, and B. Shi, A comparative study of local and nonlocal Allen-Cahn equations with mass conservation, Int. J. Heat Mass Transf. **122**, 631 (2018).

[25] J. Shen, *Modeling and Numerical Approximation of Two-Phase Incompressible Flows by a Phase-Field Approach*, Lecture Note Series (IMS, National University of Singapore, 2011).

[26] R. Folch, J. Casademunt, and A. Hernández-Machado, Phase-field model for Hele-Shaw flows with arbitrary viscosity contrast I. Theoretical approach, Phys. Rev. E **60**, 1724 (1999).

[27] M. Sussman, P. Smereka, and S. Osher, A level-set approach for computing solutions of incompressible two-phase flow, J. Comput. Phys. **114**, 146 (1994).

[28] R. Chiodi and O. Desjardins, A reformulation of the conservative level set reinitialization equation for accurate and robust simulation of complex multiphase flows, J. Comput. Phys. **343**, 186 (2017).

[29] D. Jacqmin, Calculation of two-phase Navier-Stokes flows using phase-field modeling, J. Comput. Phys. **155**, 96 (1999).

[30] Z. Chai and B. Shi, Multiple-relaxation-time lattice Boltzmann method for the Navier-Stokes and nonlinear convection-diffusion equations: Modeling, analysis, and elements, Phys. Rev. E **102**, 023306 (2020).

[31] H. Wang, X. Yuan, H. Liang, Z. Chai, and B. Shi, A brief review of the phase-field-based lattice Boltzmann method for multiphase flows, Capillarity **2**, 33 (2019).

[32] Y. Qian, D. d'Humières, and P. Lallemand, Lattice BGK models for Navier-Stokes equation, Europhys. Lett. **17**, 479 (1992).

[33] S. Aland and A. Voigt, Benchmark computations of diffuse interface models for two-dimensional bubble dynamics, Int. J. Numer. Meth. Fluids **69**, 747 (2012).

[34] Y. Zu, A. Li, and H. Wei, Phase-field lattice Boltzmann model for interface tracking of a binary fluid system based on the Allen-Cahn equation, Phys. Rev. E **102**, 053307 (2020).

[35] D. Chiappini, M. Sbragaglia, X. Xue, and G. Falcucci, Hydrodynamic behavior of the pseudopotential lattice Boltzmann method for interfacial flows, Phys. Rev. E **99**, 053305 (2019).

[36] N. Ashgriz and F. Mashayek, Temporal analysis of capillary jet breakup, J. Fluid Mech. **291**, 163 (1995).